LETTER

https://doi.org/10.1038/s41586-019-1477-8

Position and momentum mapping of vibrations in graphene nanostructures

Ryosuke Senga[1], Kazu Suenaga[1]*, Paolo Barone[2], Shigeyuki Morishita[3], Francesco Mauri[4,5] & Thomas Pichler[6]

Propagating atomic vibrational waves—phonons—determine important thermal, mechanical, optoelectronic and transport characteristics of materials. Thus a knowledge of phonon dispersion (that is, the dependence of vibrational energy on momentum) is a key part of our understanding and optimization of a material's behaviour. However, the phonon dispersion of a free-standing monolayer of a two-dimensional material such as graphene, and its local variations, have remained elusive for the past decade because of the experimental limitations of vibrational spectroscopy. Even though electron energy loss spectroscopy (EELS) in transmission has recently been shown to probe local vibrational charge responses[1–4], such studies are still limited by momentum space integration due to the focused beam geometry; they are also restricted to polar materials such as boron nitride or oxides[1–4], in which huge signals induced by strong dipole moments are present. On the other hand, measurements on graphene performed by inelastic X-ray (neutron) scattering spectroscopy[5–7] or EELS in reflection[8,9] do not have any spatial resolution and require large microcrystals. Here we provide a new pathway to determine phonon dispersions down to the scale of an individual free-standing graphene monolayer by mapping the distinct vibrational modes for a large momentum transfer. The measured scattering intensities are accurately reproduced and interpreted with density functional perturbation theory[10]. Additionally, a nanometre-scale mapping of selected momentum-resolved vibrational modes using graphene nanoribbon structures has enabled us to spatially disentangle bulk, edge and surface vibrations. Our results are a proof-of-principle demonstration of the feasibility of studying local vibrational modes in two-dimensional monolayer materials at the nanometre scale.

Our starting point was the determination of the phonon dispersion in free-standing graphite and hexagonal boron nitride (hBN) flakes by obtaining momentum-resolved EEL spectra along the ΓMΓM and ΓKMKΓ directions in momentum space. The flakes had approximately 10–20 layers and were set perpendicularly to the electron beam (Fig. 1a). A series of 20 EEL spectra were recorded every 0.25 Å^{-1} along the ΓMΓM direction for both graphite and hBN flakes (left panels in Fig. 1b, c, respectively). Compared to preliminary results obtained using ±0.5 Å^{-1} momentum resolution and a focused electron beam, we can now unambiguously assign all branches of the vibrational modes[3]. The quasi-elastic line (the zero-loss peak) has been subtracted from each spectrum. (The raw EEL spectra are shown in Extended Data Fig. 1) In the top panels of Fig. 1d, e, for graphite and hBN respectively, maps of colour-coded intensity are presented together with simulated phonon dispersion curves (solid lines) consisting of transverse, longitudinal and out-of-plane optical and acoustic modes (TO, LO and ZO, and TA, LA and ZA, respectively). Also shown are phonon energies (open triangles) derived from a Voigtian line-shape analysis of each EEL spectrum (see Extended Data Fig. 2). Because these experimental phonon energies trace the simulated phonon dispersion curves well, the active vibrational modes can be directly identified and are marked (LA, LO,...) in the coloured maps. Spectra collected along the ΓKMKΓ direction are shown in Extended Data Figs. 3 and 4.

Comparing the vibrational spectra of the apolar (graphite) and the polar (hBN) material, the most important differences are seen in the first Brillouin zone: the strong peaks arising from the scattering of the LO mode in hBN (around 170–200 meV) are not observed in graphite. This confirms that apolar materials display almost no infrared-active modes because a strong dipole moment is required for the mode to be detectable by EELS in transmission or by infrared spectroscopy at the optical limit (momentum $q = 0$ Å^{-1}). On the other hand, the LA mode of graphite is already active in the first Brillouin zone and is experimentally visible as soon as $q \geq 0.75$ Å^{-1}, as in hBN. Then both the LA and LO modes become active in the second Brillouin zone, where graphite and hBN show very similar trends. These facts strongly suggest that the selection rule in outer Brillouin zones is independent of the infrared polarizability of materials.

To understand the observed EEL intensities, we express the Stokes cross-section of the scattering electrons[11–13] as:

$$\frac{\mathrm{d}^2\sigma}{\mathrm{d}\Omega\mathrm{d}\omega}(\boldsymbol{q},\omega) = \frac{4}{a_0^2}\frac{\hbar}{q^2}\sum_{\nu}\frac{1+n_{\boldsymbol{q}\nu}}{\omega_{\boldsymbol{q}\nu}}\left|\sum_{I}\frac{1}{\sqrt{M_I}}\boldsymbol{Z}_I(\boldsymbol{q})\cdot\boldsymbol{e}^{I}_{\boldsymbol{q},\nu}\mathrm{e}^{-i\boldsymbol{q}\cdot\boldsymbol{\tau}_I}\right|^2\delta(\omega-\omega_{\boldsymbol{q}\nu}) \quad (1)$$

where a_0 is the Bohr radius, $\boldsymbol{q}$ is the momentum transfer, I and ν label the atom in the unit cell and the phonon branch, respectively, $\omega_{\boldsymbol{q}\nu}$, $n_{\boldsymbol{q}\nu}$ and $\boldsymbol{e}^{I}_{\boldsymbol{q},\nu}$ are respectively the phonon frequency, occupation and polarization, and M_I and $\boldsymbol{\tau}_I$ are the atomic mass and position. The α component of the effective charge Cartesian vector $\boldsymbol{Z}_I(\boldsymbol{q})$, accounting for the charge modulation induced by the lattice vibrations, is:

$$Z_{I,\alpha}(\boldsymbol{q}) = -i\frac{V}{q}\Delta n_{I,\alpha}(\boldsymbol{q})\mathrm{e}^{i\boldsymbol{q}\cdot\boldsymbol{\tau}_I} + \frac{q_\alpha}{q}Z_I^{\mathrm{ion}} \quad (2)$$

where V is the unit-cell volume, and Z_I^{ion} ($=Z_I - Z_I^{\mathrm{core}}$), Z_I and Z_I^{core} are, respectively, the ionic, nuclear and core-electron charges. (The core electrons are the $1s^2$ states in the present case, and considered as rigid point charges in so far as their spatial extension is much smaller than $1/q$.) $\Delta n_{I,\alpha}(\boldsymbol{q})$ is the $\boldsymbol{q}$ component of the Fourier transform of the valence-electron-density response to the displacement in the α direction of the I ion (which we compute using density functional perturbation theory, DFPT, see equation (12) of ref. [10]), evaluated at the reciprocal lattice vector $\boldsymbol{G} = \boldsymbol{0}$. In this way we fully take into account the effect of valence-electron screening beyond the spherical rigid-ion approximation used in ref. [13].

The simulated EEL spectra for graphite and hBN, given in Fig. 1b, c, respectively, (right panels), show excellent agreement with the experimental spectra. Theory only misses the weak experimental intensity of the ZO mode, which could be activated by the presence of a non-zero

[1]Nanomaterials Research Institute, National Institute of Advanced Industrial Science and Technology (AIST), Tsukuba, Japan. [2]SPIN-CNR, c/o Università G. D'Annunzio, Chieti, Italy. [3]EM Research and Development Department, JEOL Ltd, Akishima, Japan. [4]Dipartimento di Fisica, Università di Roma La Sapienza, Roma, Italy. [5]Graphene Labs, Fondazione Istituto Italiano di Tecnologia, Genova, Italy. [6]Faculty of Physics, University of Vienna, Vienna, Austria. *e-mail: suenaga-kazu@aist.go.jp

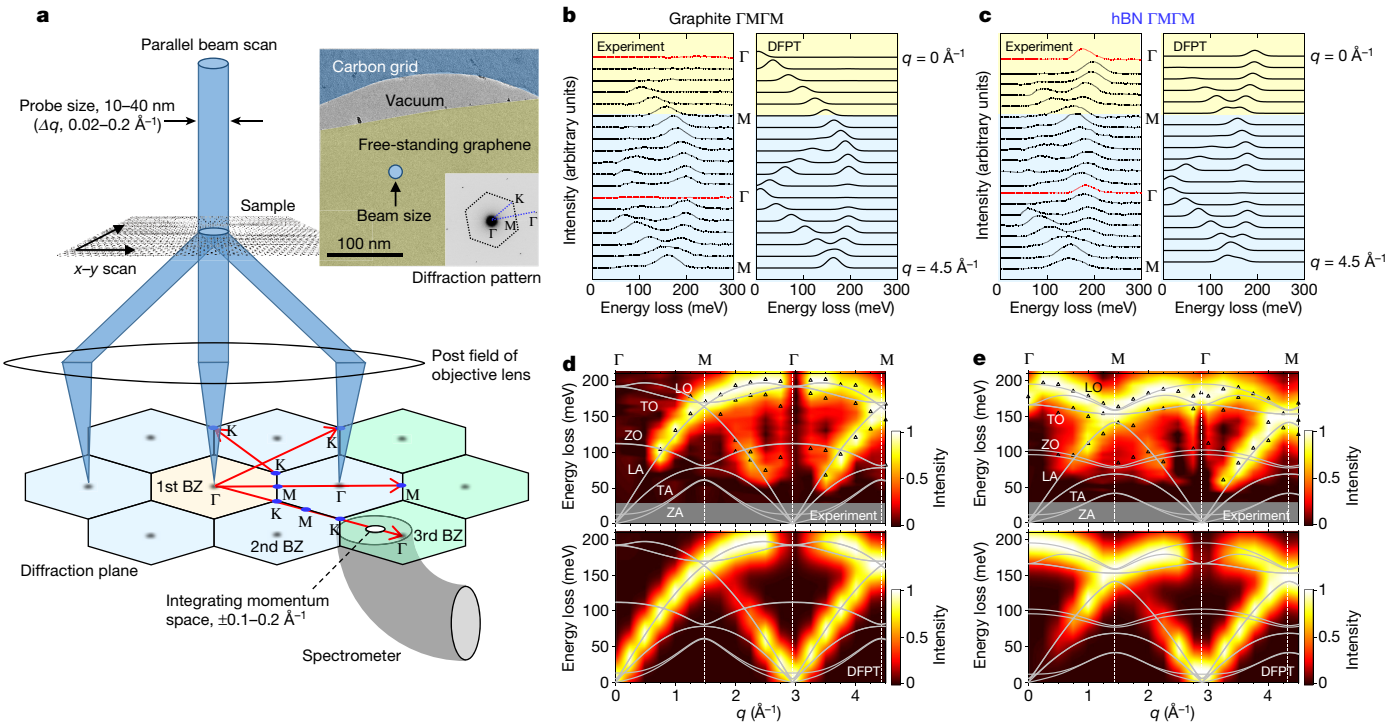

Fig. 1 | Momentum-resolved vibrational spectroscopy of graphite and hBN using EELS. a, Schematic of the experimental set-up. Inset, a typical transmission electron microscopy (TEM) image of the sample and its diffraction pattern, showing a central spot. The EEL spectra are obtained from each spot along several lines, as shown in the lower part of the main panel, with the EELS aperture focused on the diffraction plane. The post field of the objective lens and other imaging lenses were used to form a magnified diffraction pattern. **b**, **c**, Series of momentum-resolved EEL spectra for graphite (**b**) and hBN (**c**): in each panel the experimental spectra are on the left, and the simulated spectra (obtained using DFPT) are on the right. Spectra are obtained along the ΓMΓM direction (from top to bottom) for both graphite and hBN. The spectra are recorded at every 0.25 Å^{-1} from $q = 0$ to 4.50 Å^{-1} in the ΓMΓM direction, as well as at the second Γ point (2.88 Å^{-1}) of hBN. The spectra at every Γ point (red lines) include the Bragg reflection spots. **d**, **e**, Colour-coded intensity maps of graphite (**d**) and hBN (**e**), constructed from the measured EEL spectra (top) and from the simulated ones (bottom), shown with the simulated phonon dispersion curves (solid lines). Peak positions extracted from the measured spectra by line shape analysis are indicated by open triangles in the top panels. The grey regions show experimentally inaccessible energy regions where the peaks are difficult to discriminate from the quasi-elastic line. The observed redshift of the LO branch in the $q = 0$ Å^{-1} data can be explained by the suppression of LO/TO splitting occurring at the zone centre in BN slabs of finite thickness[20], which is not taken into account in our present bulk calculation.

out-of-plane momentum provided, for example, by a sample tilt (see Extended Data Fig. 5). An excellent agreement is also found for the momentum dependence of the total EEL intensity, Fig. 2a, which exhibits a very different behaviour at small q in graphite and hBN. To rationalize this finding, we analyse the momentum dependence of $\boldsymbol{Z}_I(\boldsymbol{q})$ (Fig. 2b). In the long-wavelength limit $q \to 0$, the ionic charge Z_I^{ion} is well screened by the valence density. The screening is perfect in metals and semimetals (such as graphite), so that $\lim_{q\to 0} Z_{I,\alpha}(\boldsymbol{q}) = 0$, implying a vanishing of the EEL signal. In insulators, the screening is partial and, using the expression derived by Vogl in the context of the Fröhlich interaction[14], one finds that

$$\lim_{q\to 0} Z_{I,\alpha}(\boldsymbol{q}) = q\frac{\sum_\beta Z^{\mathrm{B}}_{I,\beta\alpha} q_\beta}{\sum_{\beta,\gamma} q_\beta \epsilon^{\infty}_{\beta\gamma} q_\gamma} \qquad (3)$$

where $Z^{\mathrm{B}}_{I,\beta\alpha}$ is the Born dynamical effective charge tensor of atom I and $\epsilon^{\infty}_{\beta\gamma}$ is the high-frequency dielectric tensor. The small-momenta behaviour of the EEL intensity is hence dominated by the $1/q^2$ factor for insulators, since $\boldsymbol{Z}_I(\boldsymbol{q})$ tends to a constant value equal to the longitudinal charges measured in infrared spectroscopy[15,16]. In the opposite large-q limit, the valence screening becomes inefficient and $\boldsymbol{Z}_I(\boldsymbol{q})$ tends to the naked ionic limit Z_I^{ion} in all materials, resulting in similar EEL intensities in semimetals and insulators alike. At intermediate momenta, the effective charges display an almost linear dependence on q for both hBN and graphite (see Fig. 2b and Extended Data Fig. 6), which results in an intensity almost independent of q (Fig. 2a), irrespective of the infrared polarizability of the target material, at odds with conventional wisdom[11,13].

We now show that our large-q phonon EELS technique opens up new possibilities. Distinct phonon branches are clearly observed, depending on the q-path used in the measurements, and our technique is sensitive enough to detect phonon excitations even from a free-standing graphene monolayer. Fig. 3a–d presents phonon dispersions measured in monolayer graphene along the respective directions ΓMΓM, ΓKMKΓ, ΓK (the third-closest K to the first Γ) and KK (see Fig. 1a); the respective simulated phonon dispersions are shown in Fig. 3e–h. Although the EEL spectra (Extended Data Fig. 7) are relatively noisy compared to those of graphite, the intensity colour maps unambiguously show the phonon dispersion curves of monolayer graphene, which are consistent with the simulations for all measured directions. The LO and LA modes can be accessed along the symmetric lines (ΓMΓM (Fig. 3a, e) and ΓKMKΓ (Fig. 3b, f)), as is the case for graphite. In addition, the TA mode becomes detectable in the latter half of the second Brillouin zone along the low-symmetry line (Fig. 3c, g), owing to symmetry breaking (see also the bubble plots in Extended Data Fig. 8). Activation of the TA mode can also be observed clearly in the case of graphite (Extended Data Fig. 9). Such high sensitivity combined with flexible access to the different modes makes possible the full study of the vibrational properties of atomically thin materials. Furthermore, we obtain the dispersion along the KK direction, which cuts across the second Brillouin zone (Fig. 3d, h): we expect to see an energy drop of the LO/TO mode at the K point, namely, the Kohn

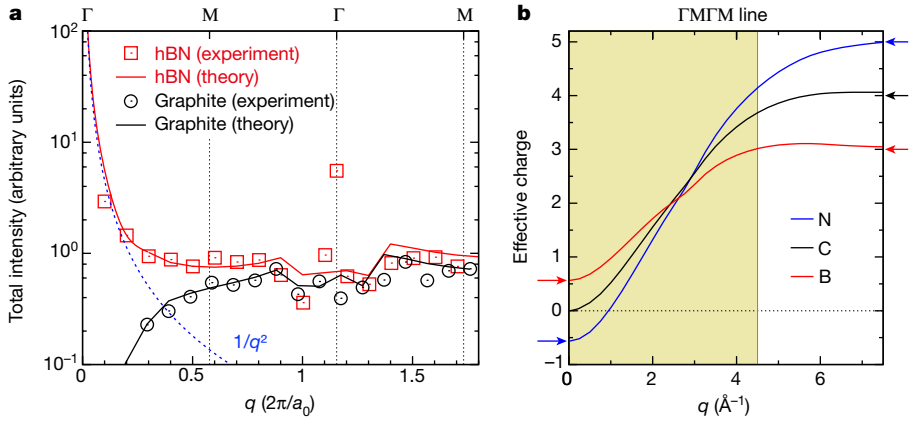

Fig. 2 | Total phonon intensity and charge modulation in EELS. **a**, The total phonon intensity of graphite (black) and hBN (red) as a function of momentum transfer q obtained from experiments (open circles and squares) and from DFPT calculations ('theory'; solid lines), evaluated as $I(\boldsymbol{q}) = \int_{\omega_{cut}}^{\infty} \mathrm{d}\omega \frac{\mathrm{d}^2\sigma}{\mathrm{d}\Omega \mathrm{d}\omega}(\boldsymbol{q}, \omega)$. To aid the comparison, a low-frequency cut-off ω_{cut}—corresponding to the grey regions in Fig. 1d, e—was assumed. A blue line scaling as $1/q^2$ is shown as a reference. **b**, Evolution of the real part of the component of effective charge parallel to momentum $\boldsymbol{q}$ evaluated along the ΓMΓM line in the polar semiconductor hBN (curves shown for boron, B, and for nitrogen, N) and in metallic graphite (curve for carbon, C). The small imaginary part is shown in Extended Data Fig. 6. The shaded area indicates the momentum range probed by the experiment, for which the total intensities shown in **a** have been measured. Arrows show the limits expected at small momentum (the longitudinal infrared charge given by equation (3)) and at large momentum (the charge of naked ions) at the left and right vertical axes, respectively.

anomaly. Instead, our experiment indicates a rather gentle energy drop of the LO/TO mode at K points in the graphene, explanation of which will entail further detailed analysis (which will require better energy and momentum resolution).

Our set-up can measure all materials with an almost negligible EELS signal delocalization effect at large-q conditions[17]: this makes truly localized measurements possible, as also demonstrated by recent work[4,18]. (We note that after submission of this work, another study[19] reported atomic-resolution EELS of the phonon density of states of an apolar material.) To further demonstrate the possibilities of local phonon probing of different vibration modes at a specific q, we performed measurements on graphene nanoribbons. The beam size in this experiment was approximately 10 nm, and the corresponding momentum resolution is ± 0.2 Å^{-1}. The sample consists of graphene nanoribbons a few tens of nanometres wide atop 18–20 graphene layers, as estimated from the annular dark field (ADF) image profile (Fig. 4). An EEL spectrum obtained at $q = 3.5$ Å^{-1} in the ΓMΓM direction is depicted in Fig. 4b. The phonon response consists of two broad peaks: peak A, between 60 meV and 100 meV, related to the LA/ZO mode; and peak B, for the LO/TO mode at about 200 meV.

Interestingly, these two signals respond differently to sample geometry (Fig. 4c–e). Whereas the LO/TO EELS intensity simply reflects the specimen thickness and is insensitive to the nanostructure of the sample, the LA/ZO signal is strongly enhanced by the presence of an edge. In addition, structural defects at impurities on the surface also yield an increased intensity of the lower-energy mode (white dashed circles in Fig. 4d). Vibrational mode mapping is also possible with confined single-layer graphene, as shown in Extended Data Fig. 10: a similar trend of edge enhancement of a specific vibrational mode is found. Hence, our experiment represents a proof of principle that

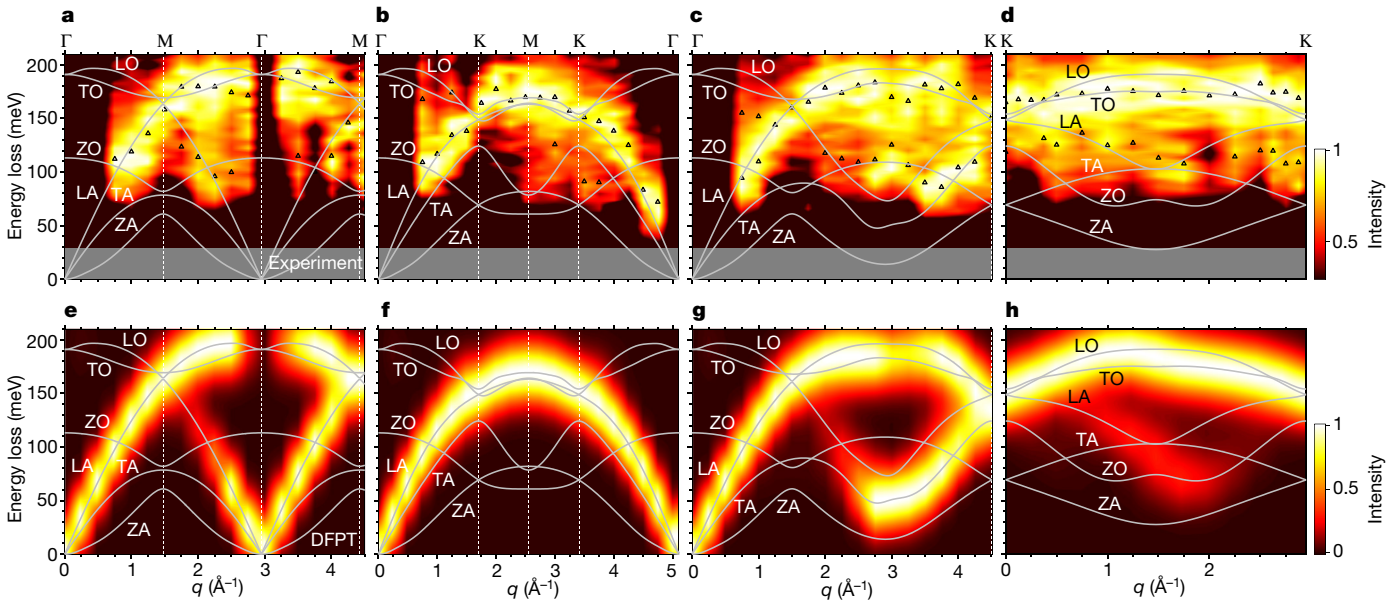

Fig. 3 | Momentum mapping of vibrations in a graphene monolayer. **a**–**h**, Maps of colour-coded intensity constructed from the measured EEL spectra ('Experiment'; **a**–**d**) and from simulated spectra ('DFPT'; **e**–**h**). Also shown are the phonon energies (open triangles) taken from monolayer graphene along the ΓMΓM, ΓKMKΓ, ΓK (the third-closest K from the first Γ) and KK directions (see also sketch in Fig. 1a). The EEL spectra in which the quasi-elastic lines have been subtracted are shown in Extended Data Fig. 7.

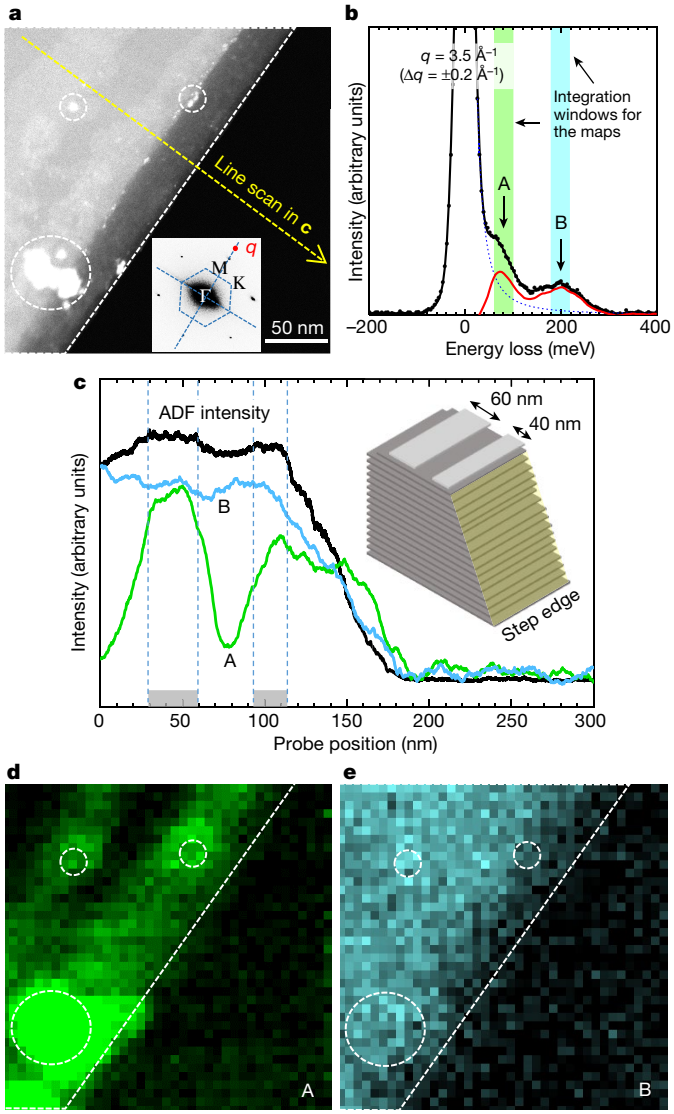

Fig. 4 | Position mapping of vibrations in graphene nanoribbons. **a**, Scanning transmission electron microscopy (STEM) image of a graphite edge with graphene nanoribbons on it; inset, its diffraction pattern. The dashed white line and circles indicate, respectively, the position of the edge and the positions of impurities, here and in **d** and **e**. The red point in the inset indicates the location of the EELS aperture at $q = 3.5$ Å^{-1}, where spectra were collected for the position mapping of vibrations. The direction of the measured q is parallel to the edge. The diffraction pattern suggests that the step edges are in the armchair direction $\langle 11\bar{2}0 \rangle$. **b**, EELS spectra and integration windows for the lower-energy mode (A; green shading) that includes LA/ZO as well as edge and sp^3 defect contributions, and for the higher-energy mode (B; blue shading) that includes LO/TO modes. **c**, Intensity profiles of the ADF image (black trace) and the lower (A; green trace) and higher (B; blue trace) energy modes. The profiles are taken along the yellow dashed line in **a**. Inset, a diagram of the edge structure along this line scan. **d**, **e**, Corresponding position mapping of vibration modes A and B, respectively.

demonstrates new possibilities in the study of local vibrational modes at the nanometre scale in monolayer 2D materials. The effective charge of atoms as a function of transferred momentum is proved here to be of primary importance when phonon scattering experiments are designed for mapping specific vibration modes. Spatially resolved and momentum-resolved measurements will in the future enable us to fully disentangle different vibrational modes and their momenta, allowing phonon dispersion to be obtained even at interfaces and edges.

Online content

Any methods, additional references, Nature Research reporting summaries, source data, extended data, supplementary information, acknowledgements, peer review information; details of author contributions and competing interests; and statements of data and code availability are available at https://doi.org/10.1038/s41586-019-1477-8.

Received: 17 December 2018; Accepted: 3 June 2019;
Published online 12 August 2019.

1. Krivanek, O. L. et al. Vibrational spectroscopy in the electron microscope. *Nature* **514**, 209–212 (2014).
2. Lagos, M. J., Trügler, A., Hohenester, U. & Batson, P. E. Mapping vibrational surface and bulk modes in a single nanocube. *Nature* **543**, 529–532 (2017).
3. Hage, F. S. et al. Nanoscale momentum-resolved vibrational spectroscopy. *Sci. Adv.* **1**, eaar7495 (2018).
4. Dwyer, C. et al. Electron-beam mapping of vibrational modes with nanometer spatial resolution. *Phys. Rev. Lett.* **117**, 256101 (2016).
5. Maultzsch, J., Reich, S., Thomsen, C., Requardt, H. & Ordejón, P. Phonon dispersion in graphite. *Phys. Rev. Lett.* **92**, 075501 (2004).
6. Mohr, M. et al. Phonon dispersion of graphite by inelastic X-ray scattering. *Phys. Rev. B* **76**, 035439 (2007).
7. Nicklow, R., Wakabayashi, N. & Smith, H. G. Lattice dynamics of pyrolytic graphite. *Phys. Rev. B* **5**, 4951–4962 (1972).
8. Vig, S. et al. Measurement of the dynamic charge response of materials using low-energy, momentum-resolved electron energy-loss spectroscopy (M-EELS). *SciPost Phys.* **3**, 026 (2017).
9. Oshima, C., Aizawa, T., Souda, R., Ishizawa, Y. & Sumiyoshi, Y. Surface phonon dispersion curves of graphite (0001) over the entire energy region. *Solid State Commun.* **65**, 1601–1604 (1988).
10. Giannozzi, P., De Gironcoli, S., Pavone, P. & Baroni, S. Ab initio calculation of phonon dispersions in semiconductors. *Phys. Rev. B* **43**, 7231–7242 (1991).
11. Van Hove, L. Correlations in space and time and Born approximation scattering in systems of interacting particles. *Phys. Rev.* **95**, 249–262 (1954).
12. Roth, F., König, A., Fink, J., Büchner, B. & Knupfer, M. Electron energy-loss spectroscopy: a versatile tool for the investigations of plasmonic excitations. *J. Electron Spectrosc. Relat. Phenom.* **195**, 85–95 (2014).
13. Nicholls, R. J. et al. Theory of momentum-resolved phonon spectroscopy in the electron microscope. *Phys. Rev. B* **99**, 094105 (2019).
14. Vogl, P. Microscopic theory of electron-phonon interaction in insulators or semiconductors. *Phys. Rev. B* **13**, 694–704 (1976).
15. Falter, C., Ludwig, W., Maradudin, A. A., Selmke, M. & Zierau, W. Valence charge density and effective charges within the density-response theory. *Phys. Rev. B* **32**, 6510–6517 (1985).
16. Ghosez, P., Michenaud, J.-P. & Gonze, X. Dynamical atomic charges: the case of ABO_3 compounds. *Phys. Rev. B* **58**, 6224–6240 (1998).
17. Muller, D. & Silcox, J. Delocalization in inelastic scattering. *Ultramicroscopy* **59**, 195–213 (1995).
18. Hage, F. S., Kepaptsoglou, D. M., Ramasse, Q. M. & Allen, L. J. Phonon spectroscopy at atomic resolution. *Phys. Rev. Lett.* **122**, 016103 (2019).
19. Venkatraman, K., Levin, B. D. A., March, K., Rez, P. & Crozier, P. A. Vibrational spectroscopy at atomic resolution with electron impact scattering. Preprint at https://arXiv.org/abs/1812.08895 (2018).
20. Sohier, T., Gibertini, M., Calandra, M., Mauri, F. & Marzari, N. Breakdown of optical phonons' splitting in two-dimensional materials. *Nano Lett.* **17**, 3758–3763 (2017).

METHODS

STEM-EELS. The momentum-resolved EELS is performed using the 'parallel-beam scanning mode', in which a parallel electron beam passes (with a convergence angle α: $0.1 < \alpha < 1$ mrad) through the sample and makes a diffraction pattern with imaging lenses (Fig. 1a). The entrance aperture of the spectrometer is placed at a given position in the diffraction plane including the first, second or third Brillouin zones and determines the momentum resolution ($\pm$0.1–0.2 Å^{-1}). The momentum range employed here ($0 < q < 5$ Å^{-1}) is almost three times wider than conventional inelastic X-ray (neutron) scattering spectroscopy or EELS in reflection, which typically probe the first Brillouin zone only. The experiments were performed using a JEOL TEM (3C2) equipped with a Schottky field emission gun, a double Wien filter monochromator and delta correctors at 30 keV. EEL spectra were collected in STEM mode, in which the energy resolution was set to 30 meV FWHM. At this energy resolution, the peaks at less than 30 meV are difficult to discriminate from the quasi-elastic line (the grey shaded region in Figs. 1d, e and 3). However, this experimentally inaccessible region also depends on the measured q. Near the Bragg reflection spots (Γ points) especially, the stronger quasi-elastic line possibly buries the lower-energy peaks. The convergent semi-angle and EELS detection semi-angles are set to 0.1 and 1.1 mrad, respectively, in Figs. 1 and 3. This condition provides a momentum resolution of $\pm$0.1 Å^{-1} and a corresponding probe size of 40 nm. Since the momentum and spatial resolutions balance each other, a smaller probe size (~10 nm) can be achieved when the momentum resolution is worsened to $\pm$0.2 Å^{-1}, as used in Fig. 4. The probe current was 10 pA. The spectra shown in this study for $q > 0.75$ Å^{-1} are constructed by summing 50 spectra in which the dwell time of each spectrum is 30 s for graphite and hBN (that is, 1,500 s per q point, Fig. 1) and 50 s for single-layer graphene (that is, 2,500 s per q point, Fig. 3). In these timescales, contamination and sample drift were hardly observed. The total acquisition times for each dispersion diagram, with up to 20 q points, were of the order of 10 h. The contribution of double scattering of the Bragg spot discussed in ref. [4] is less than 0.25% and negligible in our experiments.

Sample preparation. The graphite/graphene and hBN were mechanically exfoliated and transferred to TEM grids. The transferred samples were heated at 500 °C for 12 h in a TEM chamber.

Ab initio calculations. The effective charges defined in equation (2) and phonon dispersions in different materials were calculated within DFPT[10] as implemented in Quantum ESPRESSO[21], using the local-density approximation (LDA) and norm-conserving pseudopotentials. A $14 \times 14 \times 6$ mesh of k-points and a cut-off of 70 Ry was used for bulk hBN, while a cut-off of 90 Ry and a mesh $32 \times 32 \times 8$ ($32 \times 32 \times 1$) were used for graphite (graphene) with a Hermite–Gaussian smearing of 0.02 Ry. Phonon dispersion curves have been calculated interpolating the dynamical matrices of $12 \times 12 \times 1$ grids, while the effective charges and the EELS intensities have been evaluated for selected q-points along given directions in reciprocal space. Notice that, strictly speaking, the quantity defined in equation (2) is a complex number, even though the imaginary part is in the present cases much smaller than the real part; indeed, in all calculations we found that the former is always one order of magnitude smaller than the latter (Extended Data Fig. 6). The simulated spectra have been calculated using equation (1) and smearing the delta function with a Lorenztian broadening of 25 meV to mimic the experimental resolution.

Data availability

The datasets generated and/or analysed during the current study are available from the corresponding author on reasonable request.

Code availability

Quantum ESPRESSO is an open-source suite of computational tools available at www.quantum-espresso.org. The PH package was modified to print out the valence-electron density response to ionic displacements. The post-processing code used to simulate the EEL spectra will be included in a next release of the PH package.

21. Giannozzi, P. et al. QUANTUM ESPRESSO: a modular and open-source software project for quantum simulations of materials. *J. Phys. Condens. Matter* **21**, 395502 (2009).

Acknowledgements This work was supported by KAKENHI (17H04797 and 16H06333) and by the European Graphene Flagship Core 2 grant no. 785219. T.P. thanks the FWF for funding (P27769-N20). P.B. and F.M. acknowledge CINECA awards under the ISCRA initiative (grants HP10B3EDF2 and HP10BSZ6LY) for making available high-performance computing resources and support. We thank P. Ayala for fruitful discussions.

Author contributions R.S., S.M., T.P. and K.S. designed the experiments. R.S. performed EELS measurements. R.S. and T.P. analysed data. P.B. and F.M. established the theory and performed ab initio calculations. R.S., T.P., P.B., F.M. and K.S. co-wrote the paper. All authors commented on manuscript.

Competing interests The authors declare no competing interests.

Additional information

Correspondence and requests for materials should be addressed to K.S.

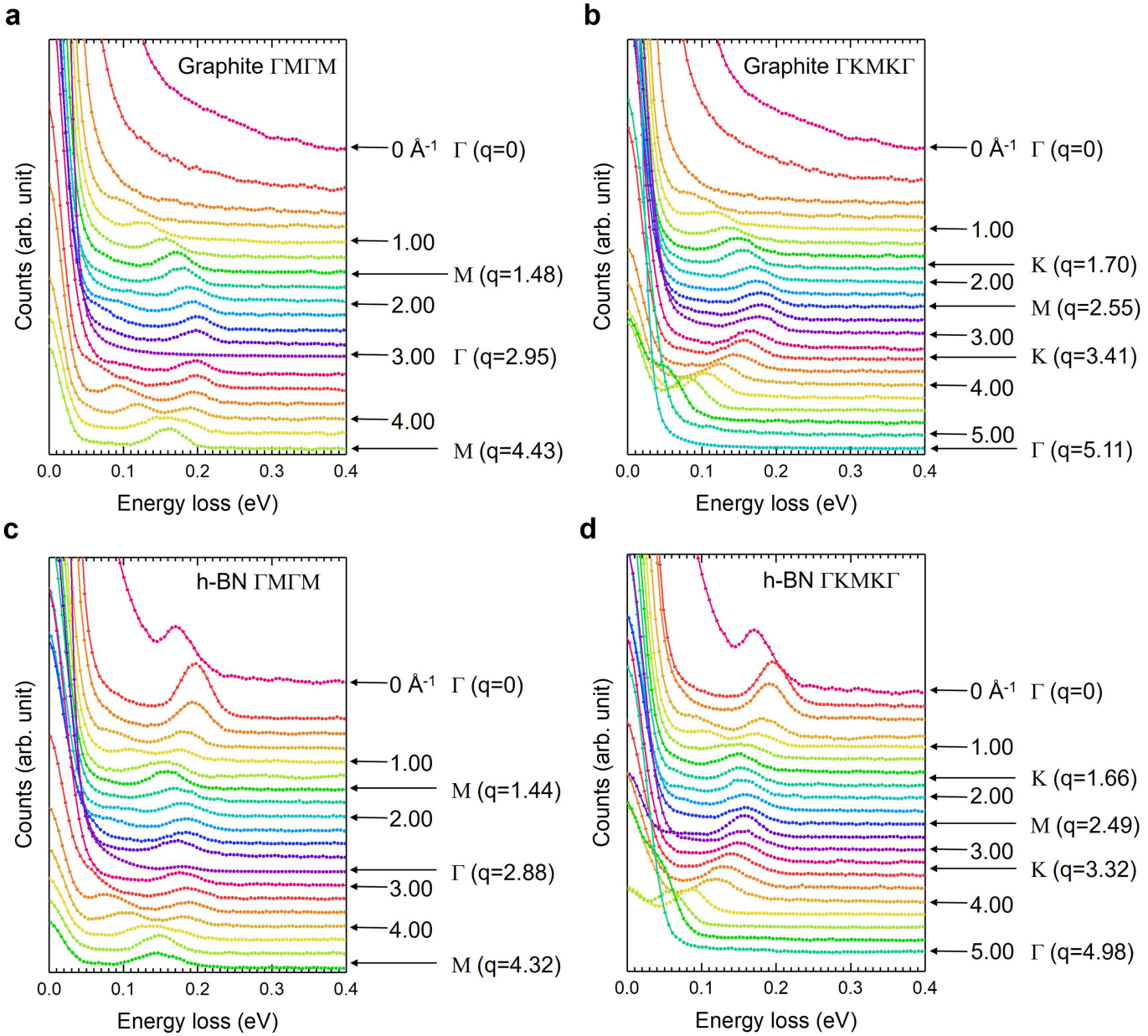

Extended Data Fig. 1 | Raw EEL spectra including quasi-elastic lines. a–d, Series of momentum-resolved EEL spectra along the ΓMΓM (**a**, **c**) and ΓKMKΓ (**b**, **d**) directions taken from graphite (**a**, **b**) and hBN (**c**, **d**) flakes.

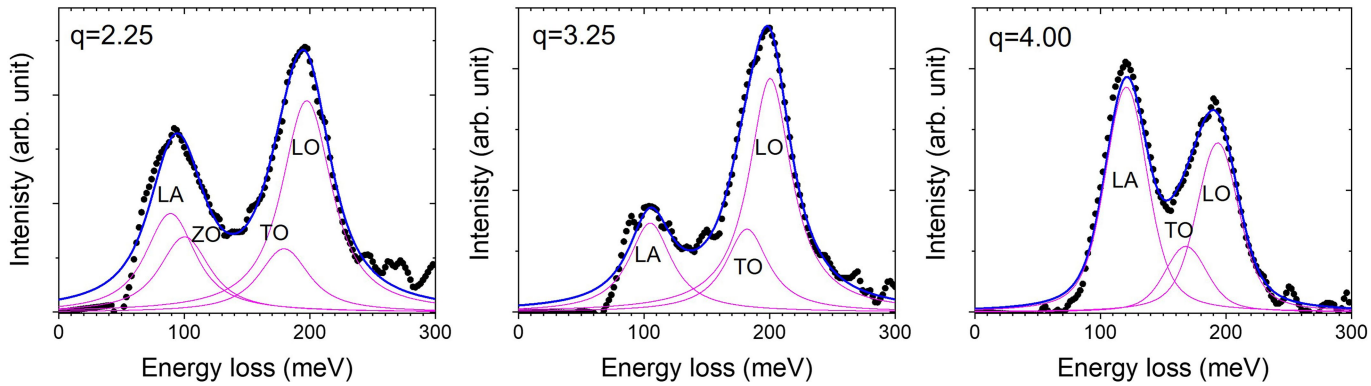

Extended Data Fig. 2 | Line shape analysis of the measured spectra of graphite. Shown are typical examples of line shape analysis of the EEL spectra of graphite at $q = 2.25$, 3.25 and 4.00 Å^{-1} (left, middle and right panels, respectively). Each component (modes LA, LO, TO, LA; purple lines) is fitted with a Voigtian including the fixed experimental broadening factor (30–40 meV). The data points and the fitting lines are shown by black dots and blue lines, respectively.

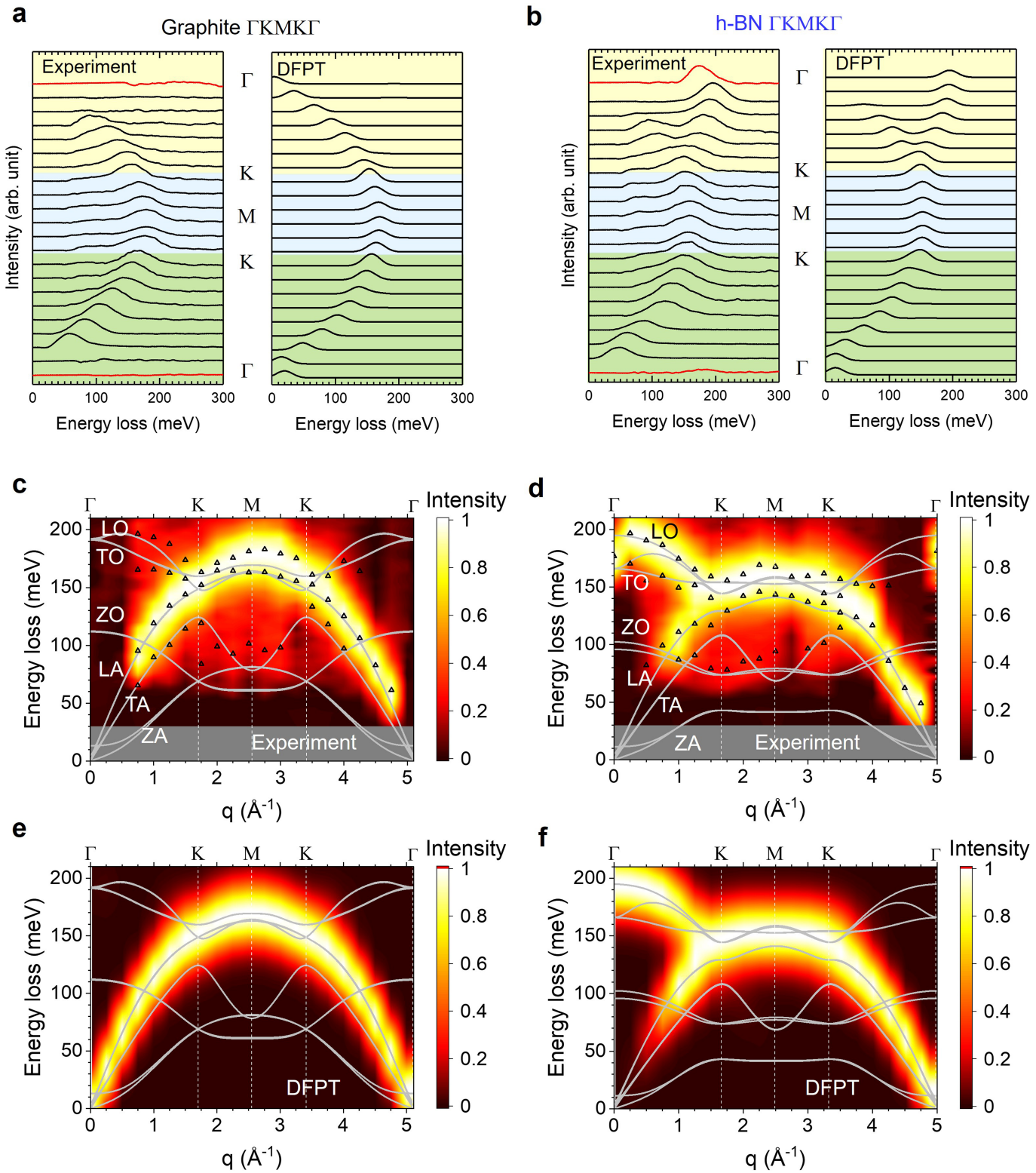

Extended Data Fig. 3 | Phonon dispersion of hBN and graphite along the ΓKMKΓ direction. a, **b**, Series of momentum-resolved EEL spectra (left) and simulated spectra (right) along the ΓKMKΓ direction (from top to bottom) for graphite and hBN, respectively. The quasi-elastic lines have been subtracted. (The raw data including the quasi-elastic lines are shown in Extended Data Fig. 1). The spectra are recorded at every 0.25 $Å^{-1}$ from $q = 0$ to 5.00 $Å^{-1}$ in the ΓM direction and at the second Γ point of graphite (5.11 $Å^{-1}$). The spectra at every Γ point (red lines) include the Bragg reflection spots. **c**–**f**, Intensity colour maps of graphite (**c**, **e**) and hBN (**d**, **f**) constructed from the measured EEL spectra (**c**, **d**) and from the simulated spectra (**e**, **f**) are shown with the simulated phonon dispersion curves (solid lines). The peak positions extracted from the measured spectra by the line shape analysis are indicated by the open triangles in **c** and **d**.

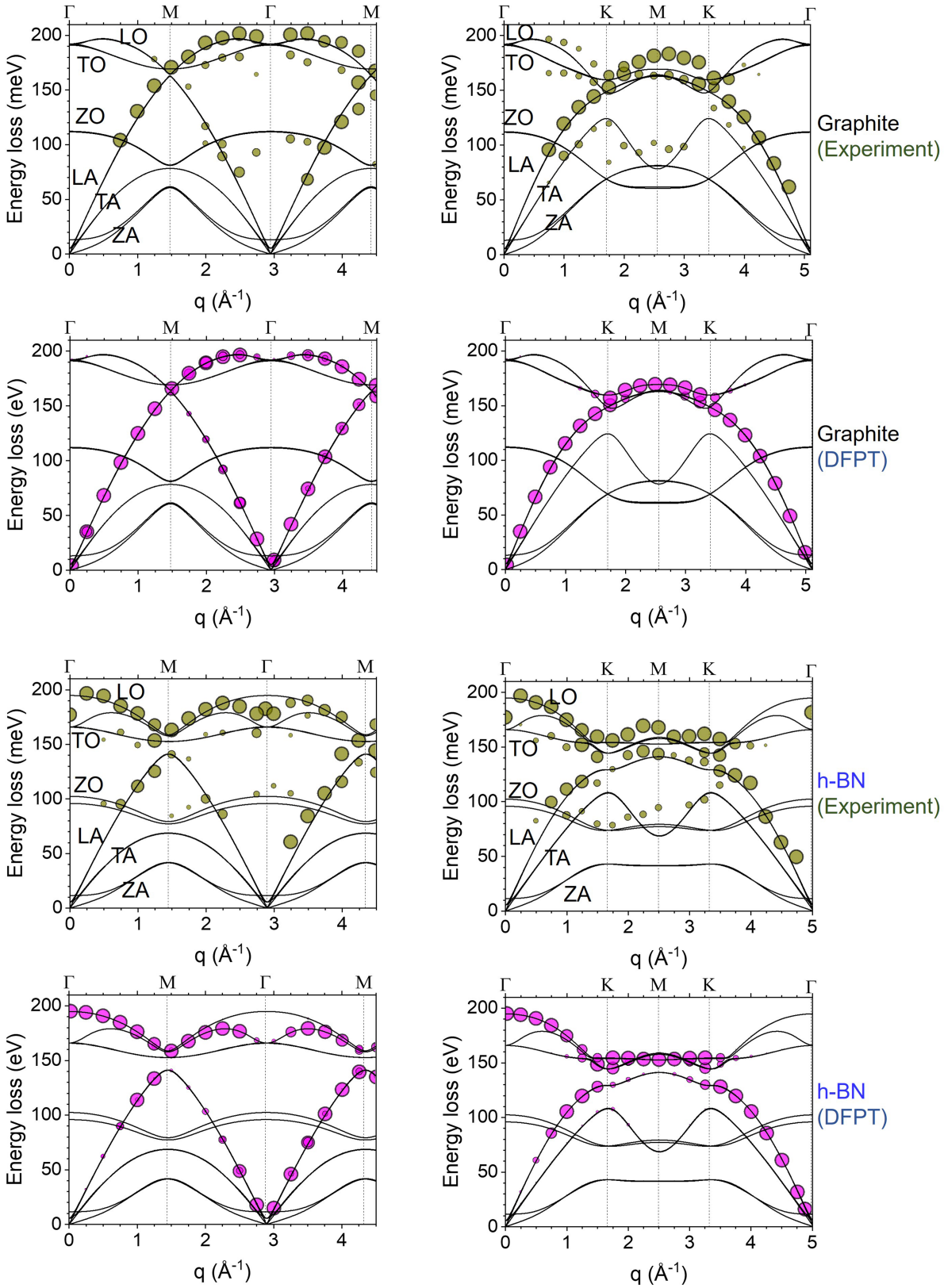

Extended Data Fig. 4 | Bubble plots of the phonon dispersion of graphite and hBN. Left column, along the ΓMΓM direction; right column, along the ΓKMKΓ direction. These plots are obtained by line shape analysis of the measured spectra ('Experiment'; first and third rows) and from the simulation (DFPT; second and fourth rows). The size (cross-section) of each point (the 'bubble') corresponds to the intensity, which is normalized by the highest peak at each measured (or calculated) q.

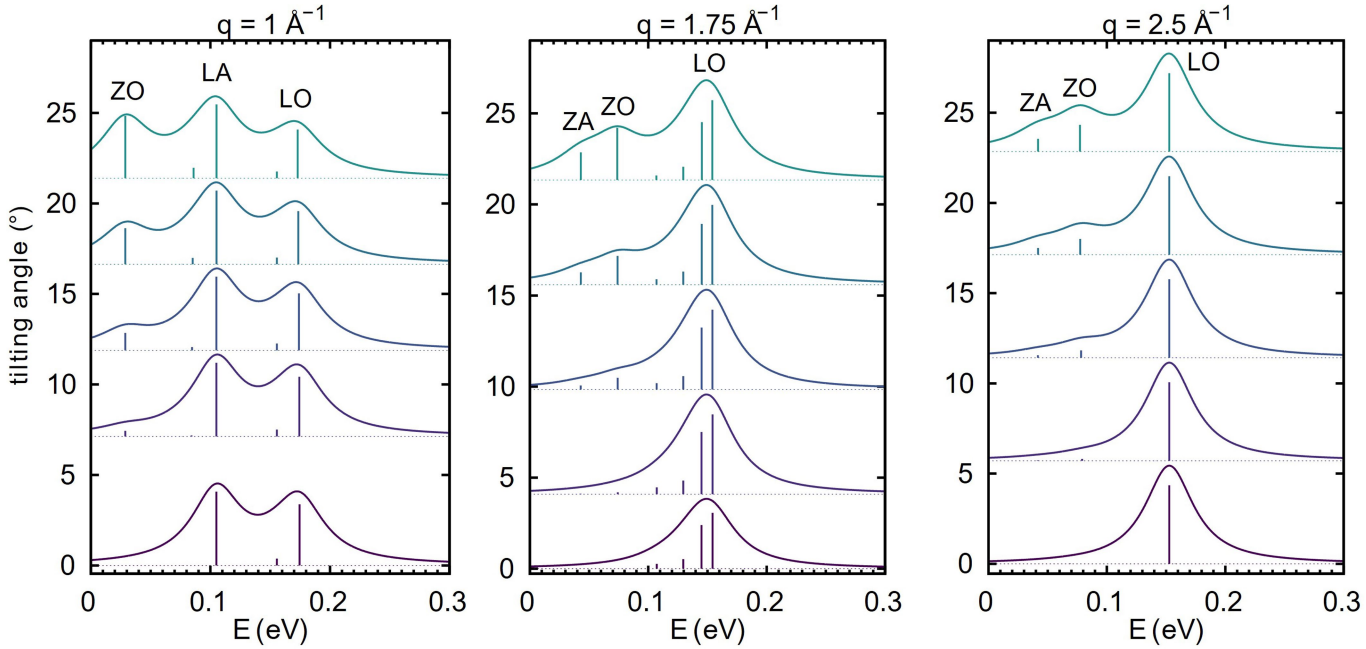

Extended Data Fig. 5 | The contribution of out-of-plane modes induced by sample tilting. Left, middle, right, simulated spectra of hBN at $q = 1$, 1.75, 2.5 Å^{-1} respectively along the ΓKMKΓ line: each panel shows the effect of the tilting angle. ZA and ZO modes are gradually activated as the tilting angle increases. Bars indicate the mode-resolved calculated intensities at each phonon frequency that are then broadened with a 25-meV Lorentzian, resulting in the simulated spectra.

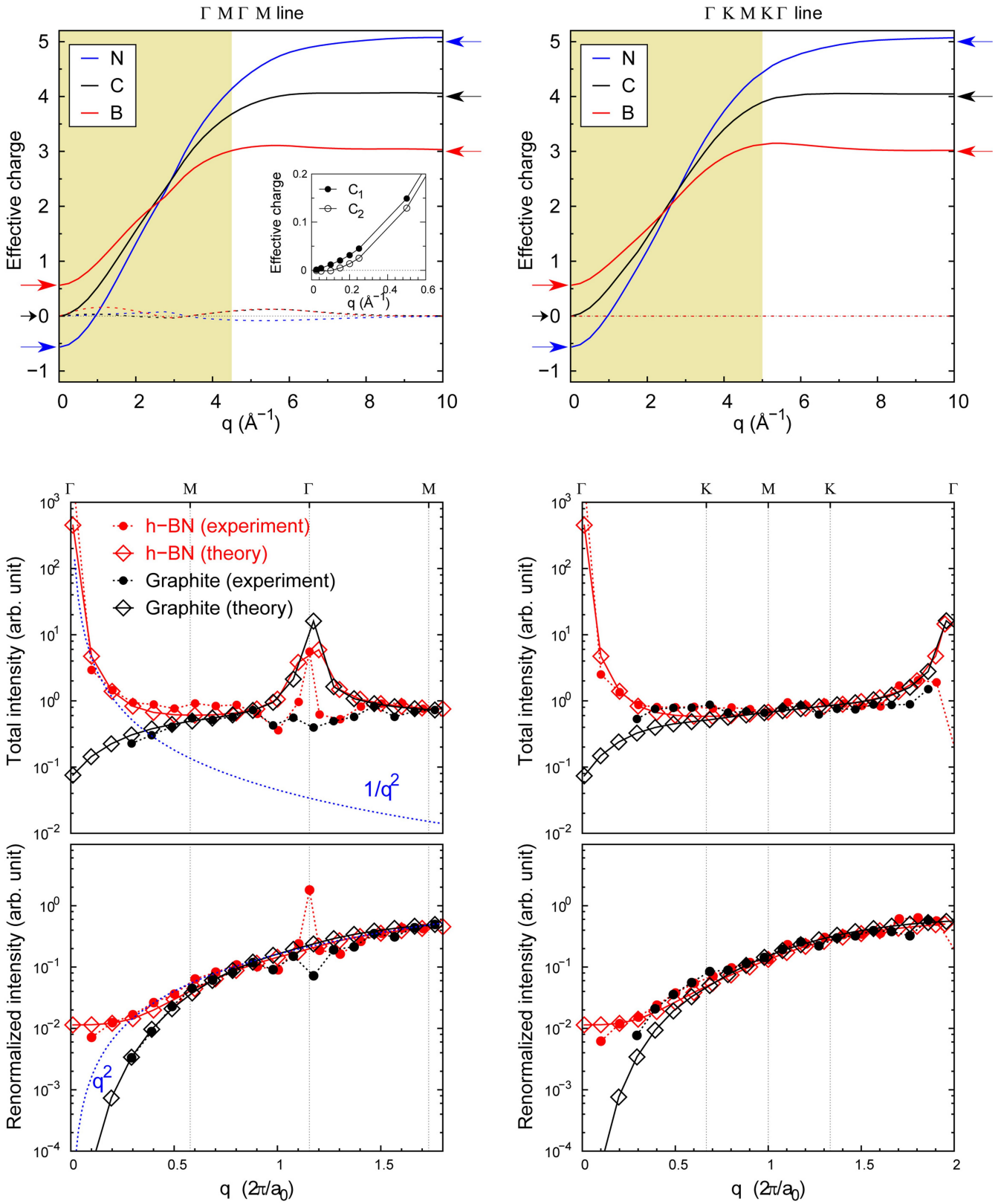

Extended Data Fig. 6 | See next page for caption.

Extended Data Fig. 6 | q-dependence of effective charges and total intensity for phonon EEL spectra. Top, the evolution of effective charges in both hBN and graphite as a function of q are shown along the ΓΜΓΜ (left panel) and ΓΚΜΚΓ (right panel) directions. Solid (dashed) lines correspond to the real (imaginary) part of the effective charge. Despite graphite hosting two inequivalent carbon ions (C_1 and C_2), their effective charges are substantially indistinguishable except for very small momenta, where tiny differences only can be seen (inset). Bottom, the total intensity for graphite (black) and hBN (red) as a function of momentum transfer obtained from the experiments (filled circles with dotted lines) and from DFPT calculations (solid lines), evaluated as $I(\boldsymbol{q}) = \int_0^\infty \mathrm{d}\omega \frac{\mathrm{d}^2\sigma}{\mathrm{d}\Omega \mathrm{d}\omega}(\boldsymbol{q}, \omega)$. The singular behaviour of the theoretical total intensity observed at Γ points in higher-order Brillouin zones can be ascribed to the $1/\omega_{\boldsymbol{q}\nu}$ dependence of the differential cross-section, which diverges for LA modes (notice that this diverging behaviour does not appear if the total intensity is evaluated with a low-frequency cut-off ω_{cut}, as shown in Fig. 2a). A renormalized intensity defined as $I(\boldsymbol{q}) \propto \sum_\nu |\sum_I \frac{1}{\sqrt{M_I}} \boldsymbol{Z}_I(\boldsymbol{q}) \cdot \boldsymbol{e}^I_{\boldsymbol{q},\nu} \mathrm{e}^{-i\boldsymbol{q}\cdot\boldsymbol{\tau}_I}|^2$ is also shown in the bottom panels. This highlights the non-trivial momentum-dependence of EEL intensity that stems from effective charges when the trivial momentum and phonon dependencies $1/q^2$ and $(1+n_{q\nu})/\omega_{q\nu}$, respectively, are neglected. A blue line scaling as $1/q^2$ (q^2) is also shown as a reference for total (renormalized) intensities.

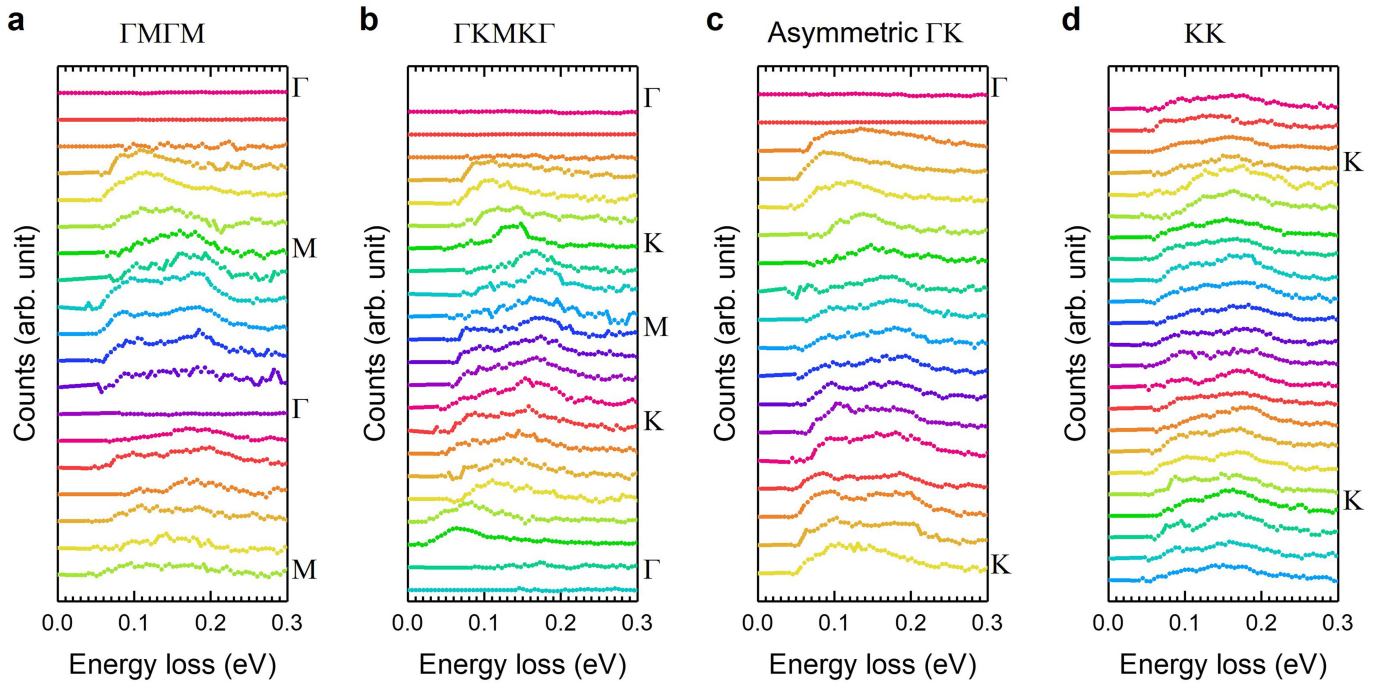

Extended Data Fig. 7 | Phonon EEL spectra of monolayer graphene. a–d, Series of momentum-resolved EEL spectra along ΓMΓM (**a**), ΓKMKΓ (**b**), asymmetric ΓK (**c**) and KK (**d**) directions taken from monolayer graphene. The quasi-elastic lines have been subtracted.

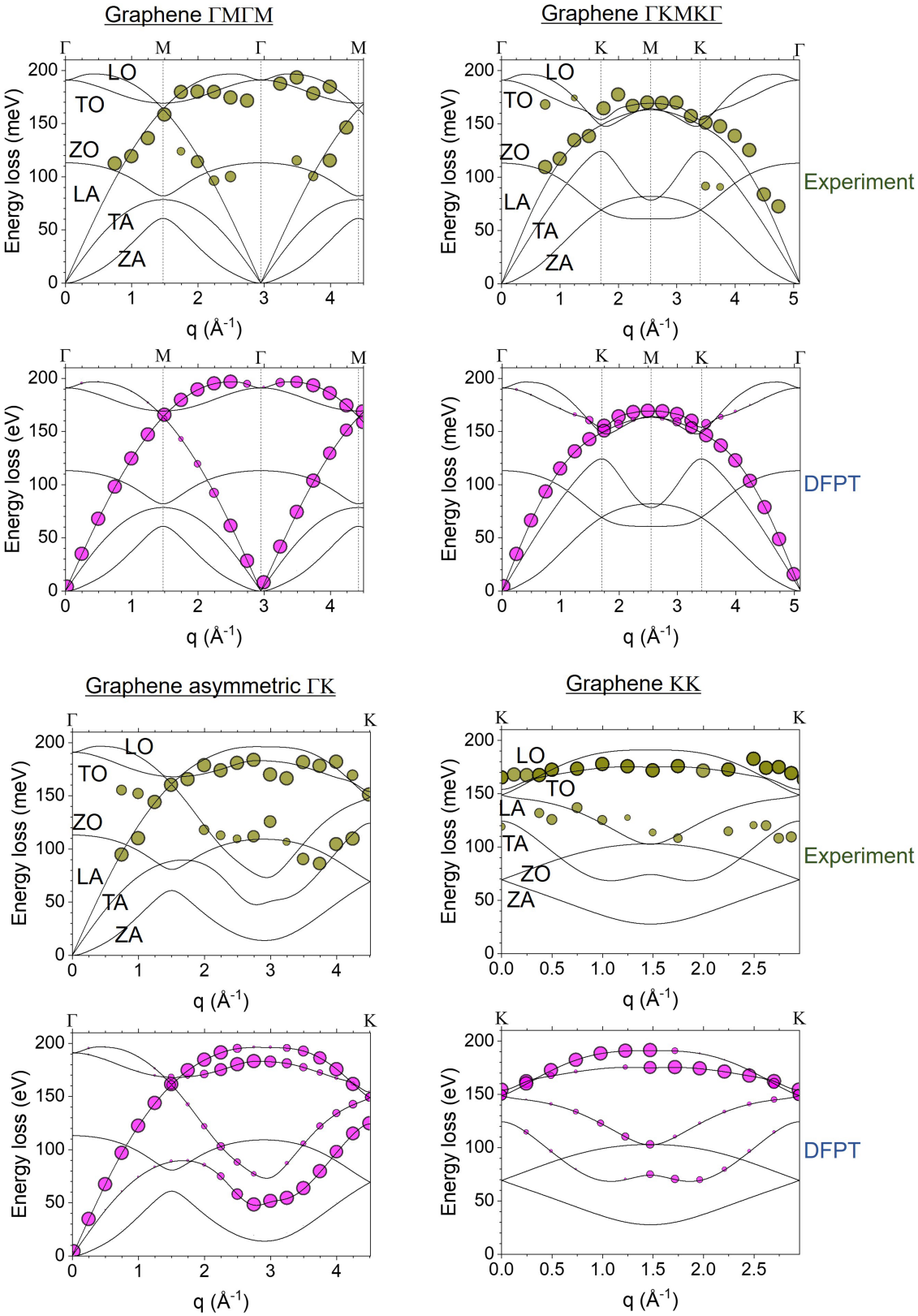

Extended Data Fig. 8 | See next page for caption.

Extended Data Fig. 8 | Bubble plots for the phonon dispersion of monolayer graphene. Each vertical pair of panels is labelled at the top by the sample material and the direction: in each of these vertical pairs, the top panel exhibits the plots obtained by line shape analysis of the measured spectra, and the bottom panel presents the plots obtained by simulation (DFPT). The directions are ΓMΓM (top left), ΓKMKΓ (top right), Γ → the third-closest K (bottom left) and KK (bottom right). The plot size (cross-section) corresponds to the intensity, which has been normalized by the highest peak at each measured or calculated q. In the ΓMΓM line, LO modes (170–200 meV) are visible at the second Brillouin zone along with LA modes that show up throughout. In the ΓKMKΓ direction, the TO mode is additionally seen at the second Brillouin zone along the KMK line for both experiment and simulation. In the low-symmetry line (Γ → the third-closest K), the TA mode shows up in the latter half of the second Brillouin zone. The dispersion along the KK direction that cuts across the second Brillouin zone shows the LO mode in the first half and the TO mode in the second half in the simulation, while this asymmetric behaviour is not clearly seen in the experiment. LA and TA modes are also activated weakly at the middle of the KK line in both experiment and simulation.

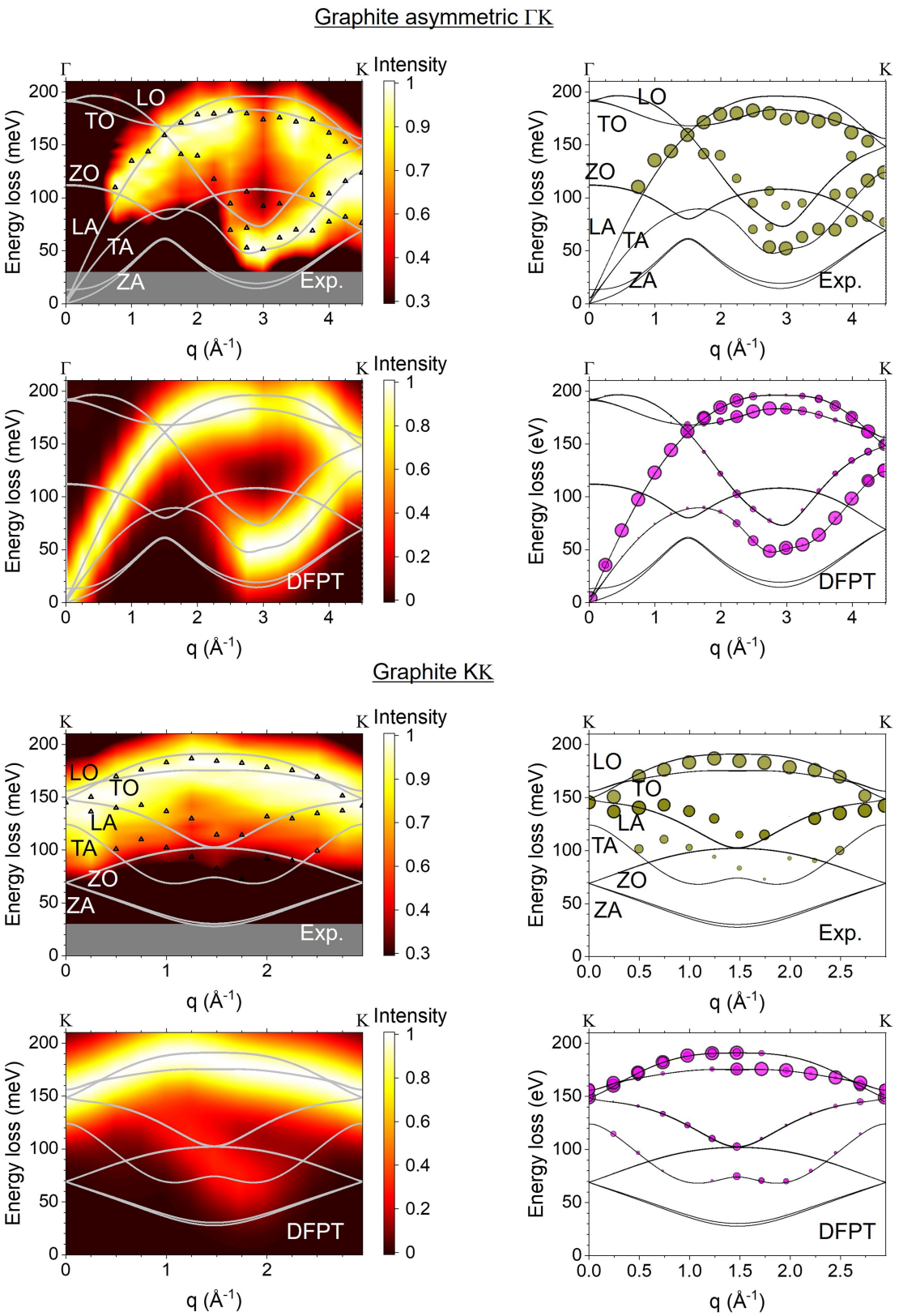

Extended Data Fig. 9 | Momentum mapping of vibrations in graphite. Shown are EELS spectra along two different directions: Γ → the third-closest K ('Graphite asymmetric ΓK'; top four panels) and KK ('Graphite KK'; bottom four panels). Within each group of four panels, the top two exhibit the intensity colour map (left) and bubble plots (right) obtained by line shape analysis of the measured spectra (Exp.): the bottom two present intensity colour maps and bubble plots obtained by the simulation (DFPT).

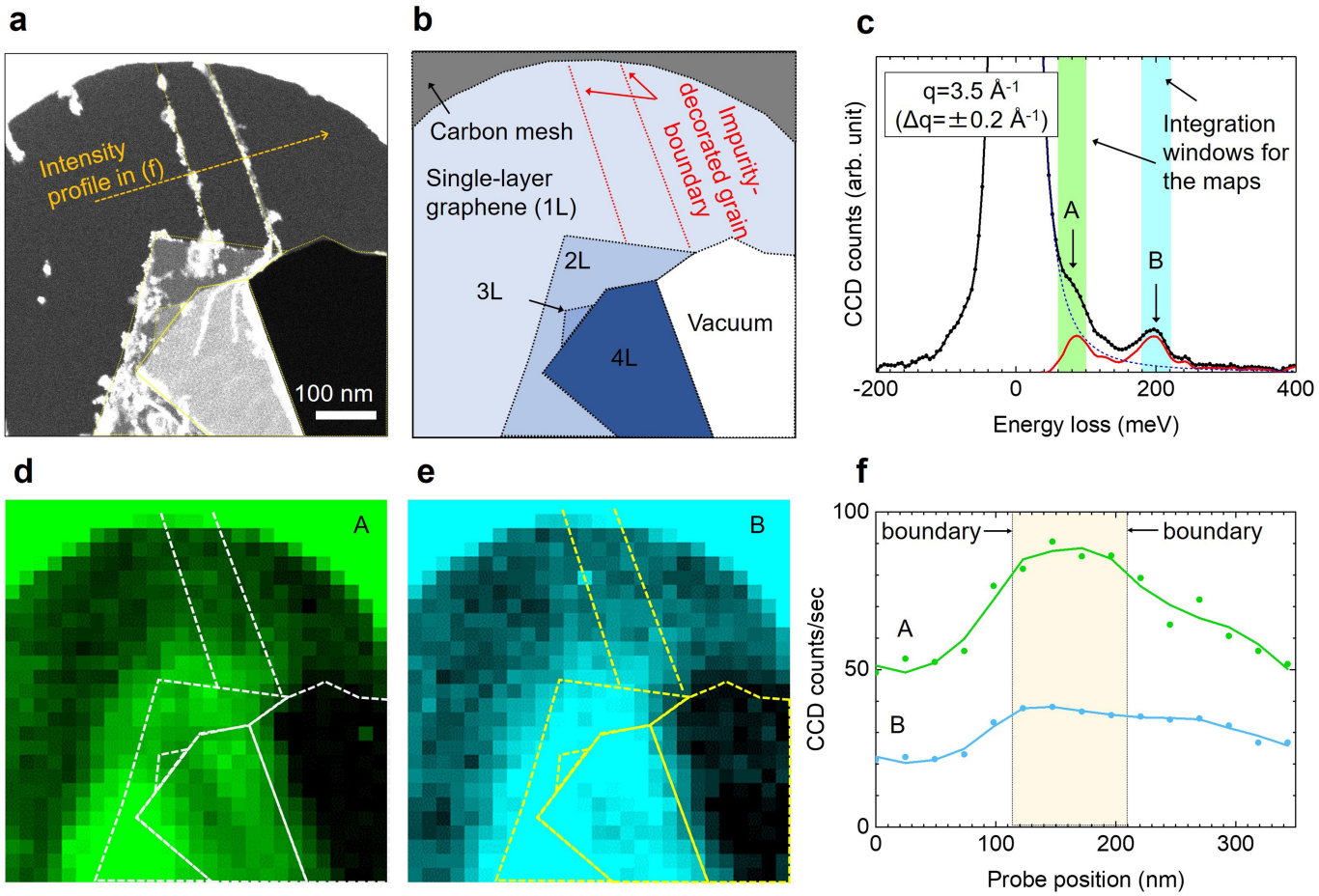

Extended Data Fig. 10 | Position mapping of vibrations in monolayer graphene. a, An STEM image of free-standing graphene; it has two-, three- and four-layer regions as well as a single-layer region (**b**). **c**, Typical EEL spectrum at $q = 3.5$ Å^{-1} taken from a clean single-layer region where 16 pixels are integrated. The phonon response there consists of two broad peaks: peak A (between 60 and 100 meV), which is related to the LA/ZO mode as well as the edge and sp^3 defect contributions; and peak B (at about 200 meV), which is related to the LO/TO mode. **d**, **e**, Corresponding position mappings of vibration modes A and B, respectively (dashed lines show information from **b**). The integration windows for the mappings are also shown by the light green and light blue stripes in **c**. **f**, Intensity profiles of vibration modes A and B along the orange line in **a** across the two impurity-decorated grain boundaries. The intensity of the LO/TO mode (B) is simply proportional to the layer number (the specimen thickness), while the lower-energy mode (A) clearly shows higher intensity at the edges of two- and four-layer regions. Interestingly, no obvious intensity enhancement can be seen at the edge of the single-layer region. In addition, we found intensity variations of the low-energy mode at grain boundaries, as shown in **f**, although their interpretation is more complicated because there must be contributions from different momentum transfers derived from domains with different orientations.